OCEANOGRAPHY

Substantially underestimated winter CO_2 sources of the Southern Ocean

Siqi Zhang[1,2]†, Peng Chen[1,2]*†, Kelsey Bisson[3], Cédric Jamet[4], Paolo Di Girolamo[5], Davide Dionisi[6], Yongxiang Hu[7], Zhenhua Zhang[1,2]*, Kun Shi[8]*, Delu Pan[1,2]

The size and control mechanism of the Southern Ocean's carbon fluxes remain highly uncertain due to sparse winter observations. Here, we integrate satellite light detection and ranging (LIDAR) measurements with machine learning to assess the Southern Ocean air-sea CO_2 fluxes between 2007 and 2020. We reveal that CO_2 outgassing south of 50°S was underestimated by up to 40% in previous studies. While the midlatitude Southern Ocean (30° to 50°S) strengthens as a carbon sink, the high-latitude region (50° to 90°S) shows Southern Annular Mode (SAM)–modulated alternation between uptake and outgassing. The air-sea CO_2 partial pressure difference (ΔpCO_2) increasingly dominates flux variability over wind-driven transfer velocity. We propose a framework involving three latitudinal loops with differing pCO_2 controls: (i) Antarctic (salinity/sea ice), (ii) polar front (atmospheric CO_2/chlorophyll), and (iii) subpolar (sea surface temperature/CO_2). The findings underscore the winter processes' critical role and necessitate year-round observations to understand Southern Ocean's global carbon cycle impact.

INTRODUCTION

The Southern Ocean (south of 35°S) plays a pivotal role in the global carbon cycle, accounting for ~40% of the ocean's anthropogenic CO_2 uptake (*1*–*3*) and serving as a critical regulator of Earth's climate system (*4*, *5*). Despite its critical role, the Southern Ocean exhibits the largest uncertainties in global estimates of air-sea CO_2 fluxes (*6*–*8*). This uncertainty originates principally from a critical scarcity of direct oceanic fugacity of CO_2 (fCO_2) measurements, exacerbated by the severely restricted ship access during austral winter (*9*–*11*). While autonomous platforms mitigate winter undersampling locally, achieving sufficient observational coverage across this vast region necessitates complementation by synoptic-scale approaches—notably, numerical modeling and satellite remote sensing. Nevertheless, both approaches are constrained by fundamental limitations in the Southern Ocean's unique physical regime.

Contemporary ocean carbon-cycle models frequently overemphasize thermally driven CO_2 partial pressure (pCO_2) variability while inadequately capturing observed seasonal fluctuations dominated by biological and physical drivers (*12*–*16*). Compounding these challenges, traditional passive ocean color remote sensing, which is essential for quantifying biological carbon uptake, becomes observationally unusable during high-latitude winters due to extended polar darkness and persistent cloud cover (*17*). This necessitates a reliance on gap-filled CO_2 flux products derived from interpolation or climatological means, rather than direct observations, thereby compounding uncertainties precisely when in situ constraints are minimal. The observational blindness of traditional methods during winter constitutes a fundamental barrier to resolving the Southern Ocean carbon cycle, a gap that the light detection and ranging (LIDAR) technology used in this study is uniquely capable of addressing.

Compounding these observational and modeling challenges, Southern Ocean air-sea CO_2 flux variability is orchestrated through a tight coupling of dynamic processes: Large-scale atmospheric forcing, dominated by the Southern Annular Mode (SAM), modulates westerly wind intensity and position. Positive SAM phases drive poleward-shifted, intensified winds that enhance upwelling of preindustrial carbon reservoirs, thereby amplifying natural CO_2 outgassing across the subpolar Antarctic zone (*18*, *19*). Ocean dynamics—notably, stratification shifts and temperature anomalies driven by broad climate modes or regional forcings—additionally regulate fluxes by modifying vertical mixing regimes and suppressing anthropogenic CO_2 absorption efficiency (*20*). Although seasonal phytoplankton blooms draw down surface pCO_2 biologically, their contribution to secular CO_2 flux trends is subordinate to dominant physical drivers and exhibits diminished multidecadal persistence (*21*). Disentangling the integrated effects of these interdependent physical-biogeochemical couplings, particularly the winter mixing/light availability/summer productivity feedback cascade, poses persistent challenges for climate models, compounding uncertainty where observational benchmarks are sparse.

Breakthroughs in spaceborne LIDAR technology now enable unprecedented year-round monitoring of the Southern Ocean carbon cycle, overcoming critical observational gaps during polar winters (*22*–*25*). Spaceborne LIDAR circumvents polar winter limitations by directly quantifying critical ocean parameters, including particulate attenuation and backscattering coefficients, and surface wind speeds independently of solar illumination, overcoming the inherent constraints of sunlight-dependent sensors (*24*, *26*–*30*). Here, we demonstrate the first year-round, LIDAR-driven assessment of Southern Ocean air-sea CO_2 fluxes by fusing Cloud-Aerosol LIDAR and Infrared Pathfinder Satellite Observation (CALIPSO) observations (2007–2020) with machine learning frameworks. Our analysis resolves

[1]State Key Laboratory of Satellite Ocean Environment Dynamics, Second Institute of Oceanography, Ministry of Natural Resources, 36 Bochubeilu, Hangzhou 310012, China. [2]Southern Marine Science and Engineering Guangdong Laboratory (Guangzhou), No. 1119, Haibin Rd., Nansha District, Guangzhou 511458, China. [3]Department of Botany and Plant Pathology, Oregon State University, 2071 SW Campus Way, Corvallis, OR, USA. [4]Université Littoral Côte d'Opale, CNRS, Université Lille, IRD, UMR 8187, Laboratoire d'Océanologie et de Géosciences (LOG), 62930 Wimereux, France. [5]Università della Basilicata, Ateneo Lucano Boulevard 10, 85100 Potenza, Italy. [6]Institute of Marine Sciences (ISMAR), Italian National Research Council (CNR), Rome–Tor Vergata, Italy. [7]NASA Langley Research Center, Hampton, VA 23681, USA. [8]Taihu Laboratory for Lake Ecosystem Research, State Key Laboratory of Lake Science and Environment, Nanjing Institute of Geography and Limnology, Chinese Academy of Sciences, Nanjing 210008, China.
*Corresponding author. Email: chenp@sio.org.cn (P.C.); zhang_zhenhua@gmlab.ac.cn (Z.Z.); kshi@niglas.ac.cn (K.S.)
†These authors contributed equally to this work.

systematic biases in legacy flux estimates induced by winter sampling gaps, while elucidating the dominant spatiotemporal heterogeneity of carbon exchange mechanisms across this climate-critical region.

RESULTS AND DISCUSSION

Substantial underestimation of the winter CO_2 source

Our LIDAR-derived year-round CO_2 flux assessments (Fig. 1) resolve distinct seasonal heterogeneity across Southern Ocean latitudes and quantify a 39.8% (±11%) underestimation of winter CO_2 outgassing inherent in traditional observation methods. Within the midlatitude band (30° to 50°S), monthly fluxes exhibit a pronounced unimodal seasonal pattern (Fig. 1A), characterized by (i) accelerated CO_2 uptake during early winter (May to July), (ii) transient attenuation in early spring (August to October), and (iii) resurgent sequestration commencing in February. This regime establishes thermodynamic controls on solubility-driven CO_2 influx as the dominant sequestration mechanism.

In stark contrast, high-latitude regions (50° to 90°S) exhibit fundamentally distinct seasonality (Fig. 1C), transitioning from a weakening carbon sink (February to June) to a persistent CO_2 source (June to October). Peak outgassing diminishes after September, yielding to resurgent carbon sequestration mediated by late-spring phytoplankton blooms. This culminates in maximum sequestration (-6.2×10^8 g of C/month) during January to February (Fig. 1D), establishing biologically driven processes as the primary control on high-latitude carbon cycling, demonstrating a marked departure from midlatitude thermodynamics-dominated regimes (*31*, *32*); specifically, variations in surface-ocean pCO_2 stemming from changes in dissolved inorganic carbon (DIC) and alkalinity are largely governed by biological activity and physical transport and mixing.

The winter data void proves critical for Southern Ocean carbon budgeting (Fig. 1C). Traditional passive sensors [e.g., Moderate Resolution Imaging Spectroradiometer (MODIS)–Aqua] fail during polar darkness, with valid observations plummeting to <50% in July and <30% in August (Fig. 1G), precisely when active LIDAR [Cloud-Aerosol LIDAR with Orthogonal Polarization (CALIOP)] maintains 63.7% coverage in ice-free zones (versus 18.7% for MODIS). These gaps spatially align with key CO_2 source regions (Fig. 1, E and F), creating systematic biases. Our LIDAR-constrained flux estimates (Fig. 1C, green line) reveal that traditional methods (purple reconstruction) underestimate winter outgassing by 40% south of 50°S (fig. S2F), although this represents just 8% of annual uptake (fig. S2E). The bias concentrates in 51° to 63°S, strongly correlated with (i) asymmetric sea ice retreat (Pacific sector dominance; fig. S2, A to D) and (ii) the 2018+ regime shift from winter source to sink (fig. S2, E and F). This undetectable sampling bias, intrinsically linked to cryosphere-atmosphere-carbon coupling, underscores the necessity for year-round active remote sensing to resolve climate-critical winter processes.

Shifting to interannual variations, our LIDAR-inclusive dataset reveals a notable strengthening of the Southern Ocean CO_2 sink from 2007 to 2020, albeit with distinct characteristics across latitudes. The midlatitude band (30° to 50°S) acts as a persistently intensifying sink, showing a steady increase in annual CO_2 uptake over the 14-year period (Fig. 1B). The high-latitude region (50° to 90°S) also exhibits an overall strengthening sink, but its trajectory is marked by far greater year-to-year variability, with temporary declines in uptake or enhanced outgassing in certain years (Fig. 1D). Critically, incorporating the previously missed winter outgassing (comparing the "total" versus "winter missing" lines in Fig. 1D) slightly dampens the overall rate of this sink intensification. This highlights the finding that a full seasonal accounting is essential not only for assessing the mean state but also for accurately quantifying long-term trends in this climate-critical region.

In conclusion, while the Southern Ocean CO_2 sink has intensified over the past 14 years, our analysis, which integrates LIDAR's unique winter observational capability, reveals contrasting seasonal mechanisms across latitudes and demonstrates that accurately capturing the magnitude of winter CO_2 outgassing is essential. The ~40% underestimation of this high-latitude winter source due to previous observational gaps significantly biases our understanding of the high-latitude region's carbon dynamics and its overall role in the global carbon budget.

Winter-resolved fluxes reveal a mosaic of latitudinal and sectoral carbon dynamics

Having established the overall temporal trends and the critical impact of winter outgassing, we now use our year-round dataset to dissect the spatial heterogeneity of these fluxes. This reveals a complex mosaic of carbon dynamics across different latitudes and ocean sectors that was previously obscured by the lack of winter data.

In the midlatitudes (30° to 50°S), our analysis confirms a persistently strong carbon sink but unveils a notable sectoral imbalance. The Indian Ocean sector emerges as a disproportionate powerhouse, accounting for 40.9% of the zonal uptake (Fig. 2B). This robust, year-round feature, now quantified with high confidence, highlights the fact that regional oceanographic features can create significant, stable heterogeneity within the broader, strengthening sink.

The true value of our winter-resolved data becomes most apparent in the high latitudes (50° to 90°S), which exhibit a dramatic seasonal reversal from a summer sink to a vigorous winter source (Fig. 2C). Our analysis reveals that this oscillation is not uniform. The Atlantic sector, despite its moderate flux amplitude, governs the majority of the variance (50.1%), acting as the region's dynamic flywheel. In contrast, the Pacific sector displays the most extreme seasonal swings, shifting from the strongest summer drawdown to significant winter emissions. Crucially, accurately capturing the magnitude of this winter outgassing in different sectors is impossible without the year-round observations provided by LIDAR, and it is this spatially variable outgassing that shapes the net annual budget of the high-latitude system.

In summary, the Southern Ocean carbon sink is not a monolith. It is a mosaic of distinct regional systems operating under different rules. The clear resolution of this spatial complexity, particularly the contrasting winter behaviors in the high-latitudes, is a prerequisite for understanding the mechanistic drivers discussed next. This underscores the fact that resolving the Southern Ocean carbon cycle requires accounting not only for winter but also for its profound spatial variations.

Drivers of Southern Ocean CO_2 flux dynamics

The air-sea CO_2 flux emerges from the multiplicative interaction of three fundamental components: the gas transfer velocity (k_w), CO_2 solubility (sol), and the air-sea partial pressure difference (ΔpCO_2; hereafter denoted as d_p) (*33*). To find out the mechanistic controls on Southern Ocean carbon flux variability, we conducted a principal driver analysis focusing on the two most dynamic parameters, k_w

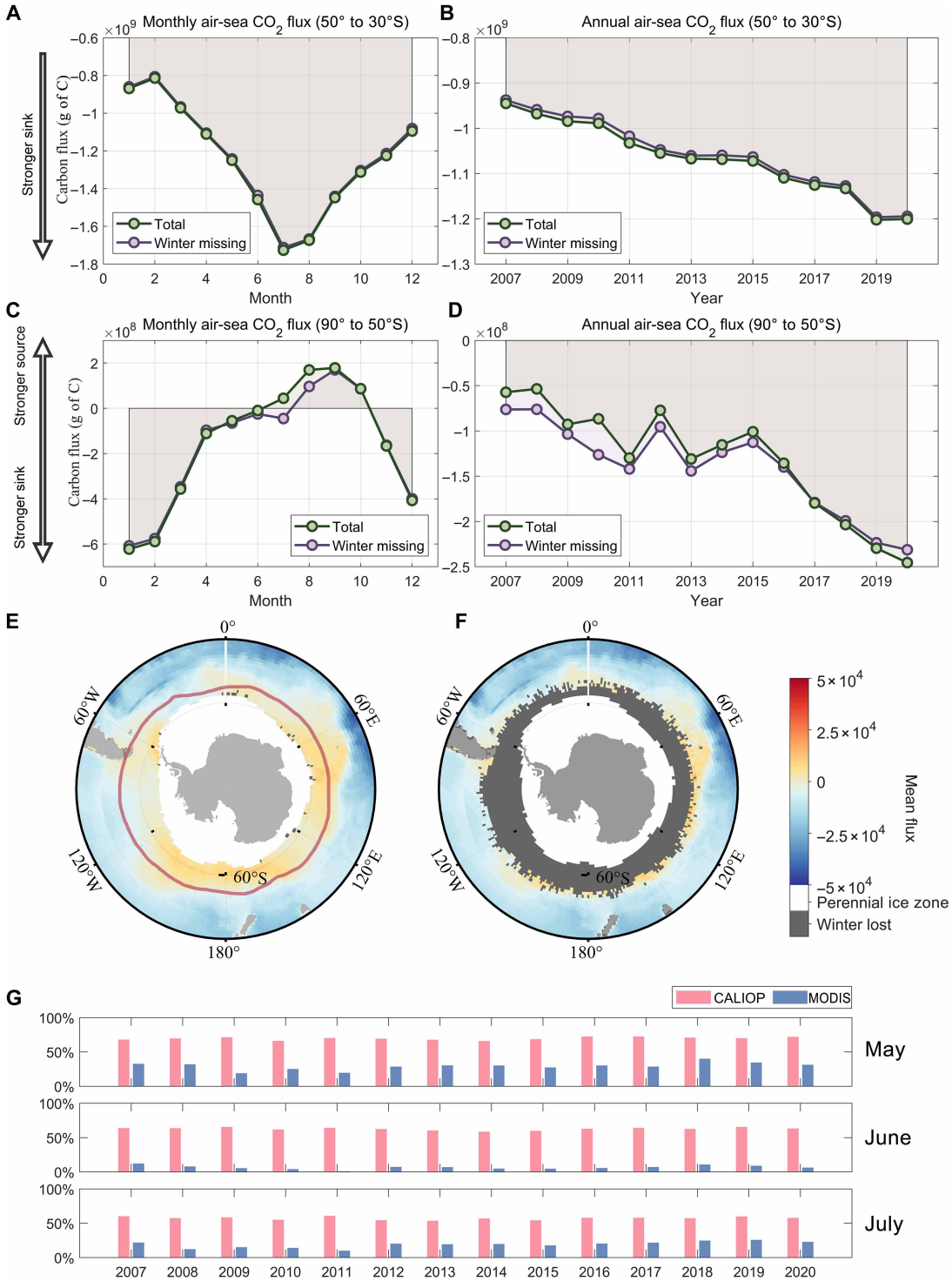

Fig. 1. Impact of winter observational gaps on Southern Ocean air-sea CO_2 flux estimates (2007–2020). (**A** and **B**) Mean monthly (A) and total annual (B) integrated CO_2 flux for the midlatitude zone (30° to 50°S). (**C** and **D**) Mean monthly (C) and total annual (D) integrated CO_2 flux for the high-latitude zone (50° to 90°S). In all line plots, green lines ("total") are flux estimates from our year-round, LIDAR-inclusive dataset. Purple lines ("winter missing") are from a simulated dataset that mimics the winter data gaps of traditional passive sensors. Negative values indicate ocean uptake (a stronger sink). The separation between the "total" and "winter missing" lines is mainly concentrated during June to October, corresponding to the high-latitude winter. (**E**) Map of the mean annual air-sea CO_2 flux density from our "total" analysis. (**F**) Map identifying regions of persistent winter data loss for passive sensors (gray shading, "winter lost") and the perennial sea ice zone. The red outline in (E) denotes the "winter lost" area from (F). (**G**) Winter observation coverage for active (CALIOP) versus passive (MODIS) sensors. Together, the panels demonstrate that winter data gaps [(G) and (F)] lead to a substantial underestimation of CO_2 outgassing [divergence between lines in (C)], a bias corrected by LIDAR.

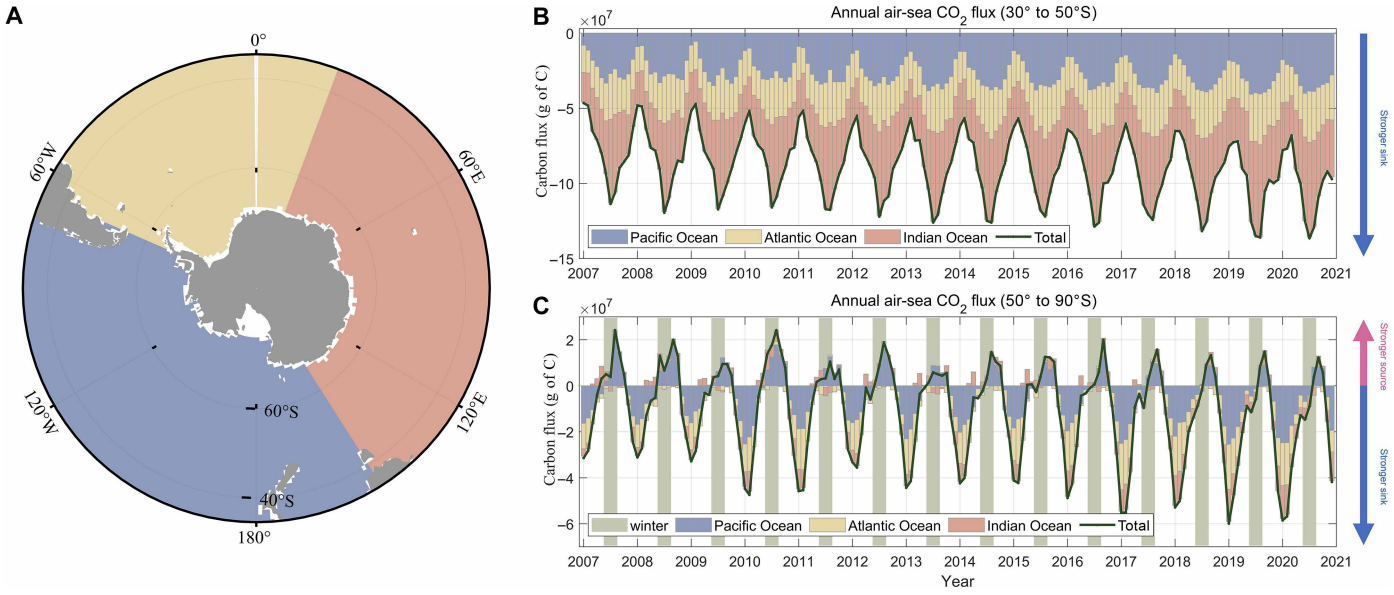

Fig. 2. Sectoral and latitudinal breakdown of Southern Ocean air-sea CO_2 fluxes. (**A**) Map defining the geographical boundaries of the Pacific (blue), Atlantic (yellow), and Indian (red) sectors. The Pacific sector is defined as 147°E to 67°W, the Atlantic sector as 67°W to 20°E, and the Indian sector as 20° to 147°E. (**B** and **C**) Monthly time series of integrated air-sea CO_2 flux for the midlatitude (30° to 50°S) and high-latitude (50° to 90°S) zones, respectively. Stacked areas show contributions from each sector, and the solid black line is the total flux. In (C), green shading highlights the austral winter period (June to October), when the high-latitude region becomes a net CO_2 source. Negative values signify ocean uptake (sink); positive values signify outgassing (source).

(wind speed–dependent turbulent gas exchange) and d_p (thermodynamic forcing and surface ocean biogeochemical forcing), which exhibit distinct spatiotemporal signatures. The air-sea CO_2 exchange is primarily controlled by the gas transfer velocity (k_w) and the concentration gradient dynamics at the air-sea interface, as indicated by d_p variations.

While pressure difference forcing (d_p) governs flux magnitude across most Southern Ocean regimes, turbulent gas exchange (k_w) emerges as the principal control within a circumpolar band (~45° to 60°S). The k_w-dominated belt coincides with the Southern Ocean's wind-stress maximum yet functions as a biogeochemical pivot; its characteristically weak mean d_p renders carbon fluxes disproportionately responsive to perturbations in wind-forced gas transfer. This regional dichotomy underscores how the relative dominance of thermodynamic and biogeochemical (d_p) versus mechanical (k_w) drivers shifts latitudinally, creating a mosaic of carbon sink-source sensitivities.

Temporally, the Southern Ocean exhibits comparable spatial footprints for k_w-dominated and d_p-dominated flux variability regimes, each spanning ~50% of the domain annually. A marked seasonality governs these patterns: Gas transfer velocity (k_w) peaks in influence during austral autumn (54% coverage in May), while pressure difference forcing (d_p) reaches maximal extent in summer (56% in December; Fig. 3B). Critically, our analysis reveals a multidecadal trend (2007–2020) wherein d_p-controlled area expanded steadily from 51 to 60%, indicating a fundamental shift toward air-sea partial pressure gradients as the principal modulator of Southern Ocean carbon flux variability.

Building on the Southern Ocean's established climate linkages, we quantify how the SAM, the dominant extratropical climate mode, modulates CO_2 flux dynamics through its dual control of gas transfer velocity (k_w) and partial pressure gradient (d_p). Detrended, deseasonalized analyses reveal SAM-index covariation with air-sea CO_2 flux anomalies (Fig. 3C), where positive phases systematically reduce carbon uptake (or enhance outgassing), exemplified during 2008, 2010, and 2015–2016. This reflects SAM's wind-mediated forcing: Intensified westerlies during positive phases amplify Ekman-driven northward transport within the Antarctic Circumpolar Current's southern flank (*18*, *34*). The SAM-driven upwelling of DIC-enriched waters overwhelms the biological pump's sequestration capacity, triggering net CO_2 outgassing, a mechanistic asymmetry most acute poleward of 50°S. Connections emerge clearly in the observational record: Negative SAM states (e.g., 2009 and 2013) systematically strengthen the Southern Ocean's carbon sink, while the high-latitude belt (50° to 90°S) exhibits greater SAM-linked flux variability than subpolar zones, underscoring latitudinal gradients in air-sea coupling efficiency.

Mechanistic dissection of SAM's flux modulation reveals divergent driver behaviors: The partial pressure gradient (d_p) exhibits robust covariation with annular mode phases (Fig. 3D), where negative SAM states induce CO_2 uptake surges following ~4-month lags (e.g., 2009 and 2020), while positive phases drive near-synchronous oceanic outgassing (2010 and 2015–2018). Wind-mediated gas transfer velocity (k_w) anomalies dynamically track SAM polarity (Fig. 3E), yet detrended analyses demonstrate that, compared to d_p, k_w has a substantially smaller interannual amplitude, exhibiting merely one-third the variability of d_p forcing, establishing the former as the primary determinant of net carbon flux sensitivity to annular mode variability.

These findings establish the SAM as a dual modulator of Southern Ocean carbon fluxes, operating through both physical (gas transfer velocity, k_w) and biogeochemical (partial pressure gradient, d_p) pathways. The emergent dominance of d_p variability, with its persistent SAM covariance despite temporal lags, highlights climate-driven pCO_2 redistribution as the sustained governor of regional

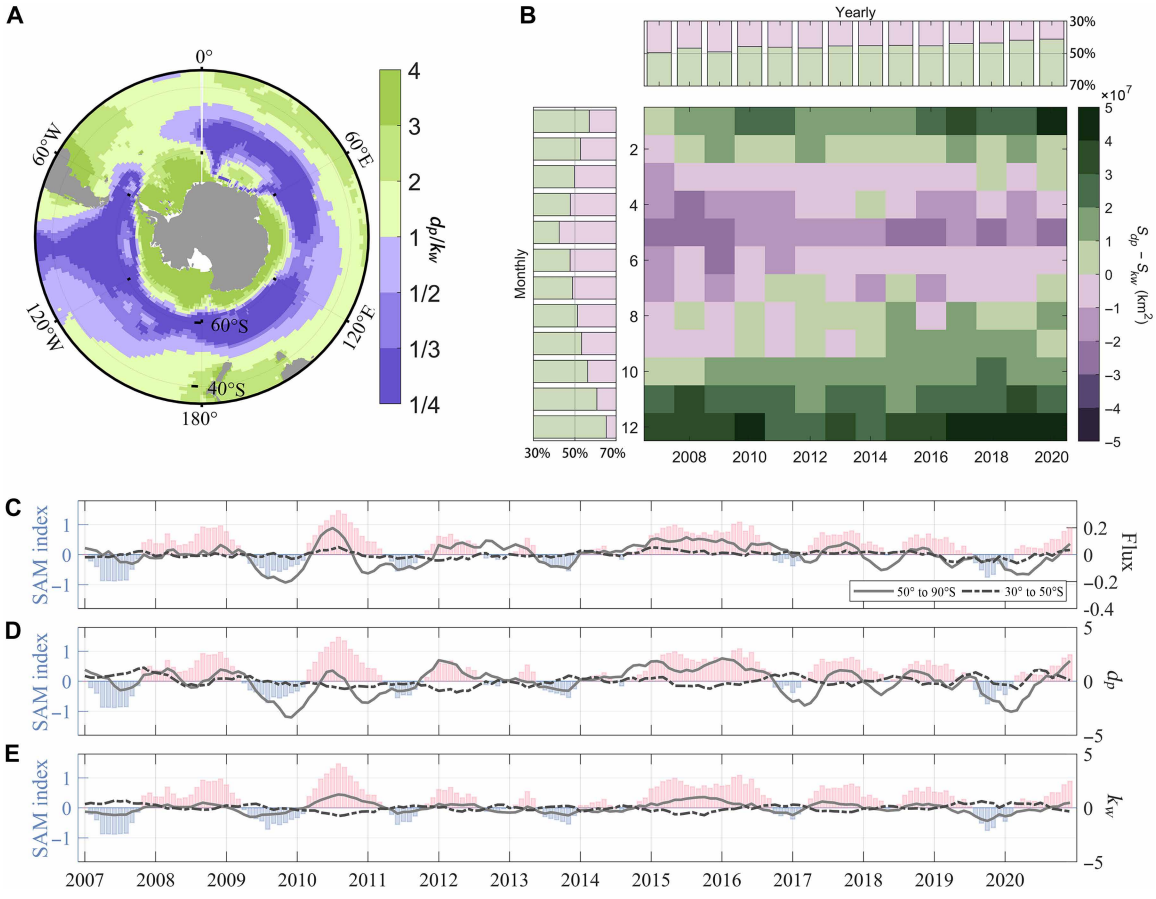

Fig. 3. Spatiotemporal variability in CO_2 flux drivers and their relationship with the SAM. (**A**) Spatial map of the dominant driver of CO_2 flux variability, determined by the ratio of gas transfer velocity (k_w) to the air-sea pCO_2 difference (d_p). Green indicates d_p dominance; purple indicates k_w dominance. (**B**) Evolution of the fractional area controlled by k_w versus d_p (2007–2020). (**C** to **E**) Comparison of the SAM index (pink/blue bars, 3-month running mean) with deseasoned and detrended anomalies in (C) net CO_2 flux, (D) d_p, and (E) k_w.

carbon sequestration capacity. This mechanistic hierarchy proves most acute in the high-latitude Southern Ocean, where amplified sensitivity to annular mode variability cements the region's disproportionate influence on global carbon-climate coupling.

Control mechanisms of Southern Ocean pCO_2

To elucidate the dominant controls on surface seawater partial pressure of CO_2 (pCO_2), a prerequisite for resolving Southern Ocean carbon dynamics beyond flux variability driven by air-sea pCO_2 gradients (ΔpCO_2), we applied random forest (RF) regression to quantify the relative influences of key environmental drivers across heterogeneous regimes. This analysis deconvolved contributions from sea surface temperature (SST), sea surface salinity (SSS), sea ice concentration (SIC), chlorophyll-a (Chl-a) concentration, mixed layer depth (MLD), sea surface height (SSH), sea surface wind speed (SSW), and atmospheric column-averaged dry-air mole fraction of carbon dioxide (xCO_2) to observed spatiotemporal pCO_2 variability.

Our analysis reveals distinct zonal patterns in pCO_2 drivers, with dominant controls shifting progressively by latitude (Fig. 4A). Spatial distributions of relative importance coefficients for primary and secondary controls appear in Fig. 4B (top factors; white-masked where coefficients are <0.5) and Fig. 4C (secondary factors), with dashed lines approximating interregional boundaries. Synthesizing these patterns, we propose a "three-loop pattern" hypothesis, three latitudinally structured dynamic regimes (north to south), each defined by unique primary and secondary controls (Fig. 4).

Subpolar loop (~north of 45°S)

SST dominates as the primary control (highest importance; Fig. 4B), reflecting temperature-driven CO_2 solubility. Atmospheric xCO_2 acts secondarily (Fig. 4C), modulating air-sea exchange via diffusion/uptake. Warmer SST reduces CO_2 uptake in northern subduction zones and alters outflow patterns where circulation or biology govern fluxes.

Polar front loop (~45° to 60°S)

xCO_2 is the primary driver (Fig. 4B), enhancing CO_2 absorption and elevating surface pCO_2. While high xCO_2 may stimulate phytoplankton growth, nutrient constraints limit this effect. Chlorophyll concentration (Chl) emerges as the secondary control (Fig. 4C). Episodic blooms, fueled by upwelling and frontal dynamics, drive localized pCO_2 drawdown, consistent with enhanced high-latitude productivity under elevated CO_2 (*35*–*37*). Atmosphere-biology coupling generates complex feedback across sharp hydrographic transitions.

Antarctic loop (~south of 60°S)

SSS dominates as the primary pCO_2 control (Fig. 4B), modulating carbon chemistry via freshwater fluxes from precipitation and ice melt/formation. SIC acts as the key secondary driver (Fig. 4C), governing

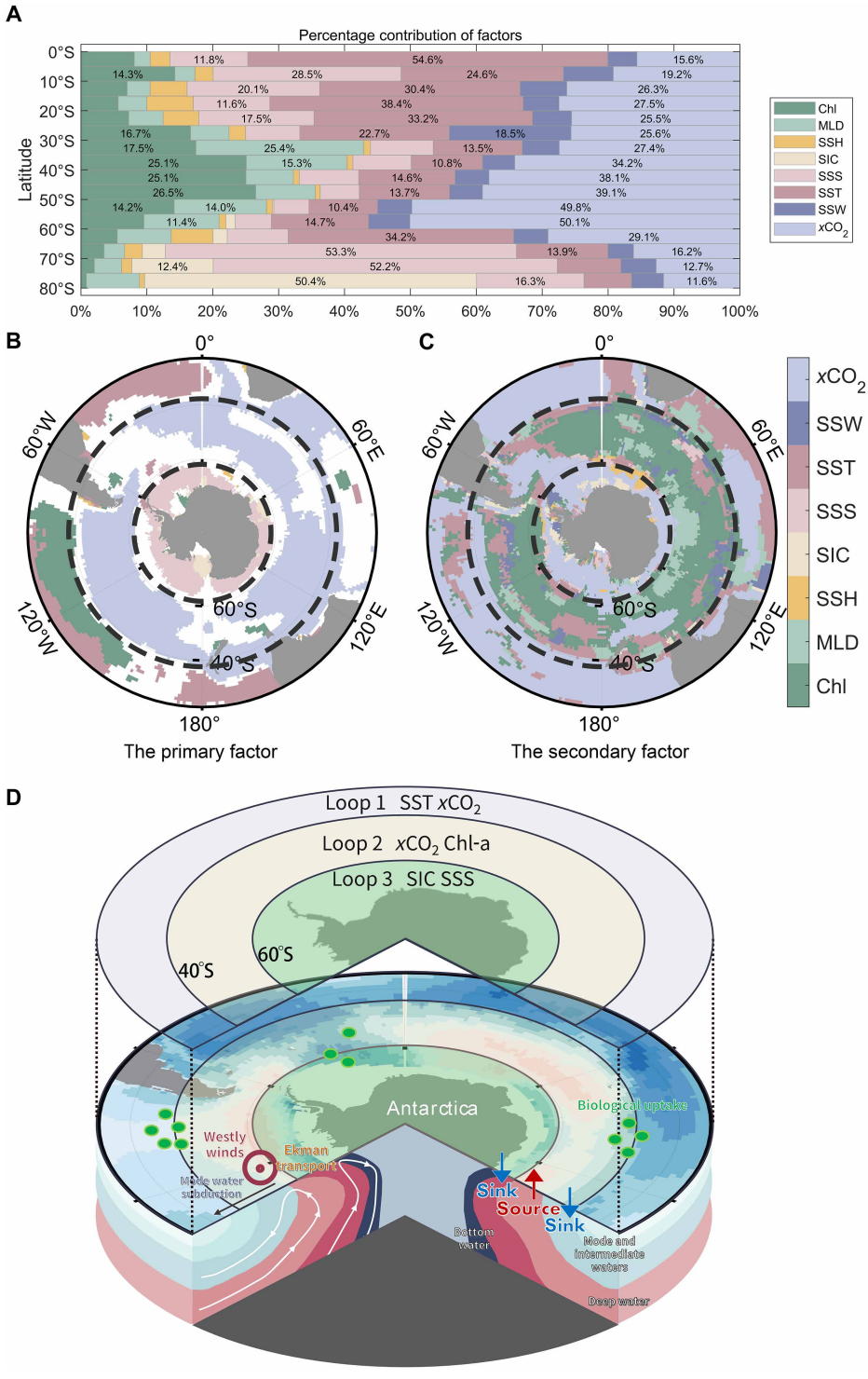

Fig. 4. Spatial patterns of surface pCO_2 drivers and the proposed three-loop framework. (**A**) Latitudinal variation in the percentage contribution of key environmental drivers to surface pCO_2 variability. (**B** and **C**) Spatial maps identifying the primary (B) and secondary (C) drivers of pCO_2 variability. Dashed lines delineate the approximate boundaries of the three proposed loops. In (B), regions where the primary driver's importance is below 50% are masked white. (**D**) Schematic of the proposed three-loop conceptual framework, illustrating the hypothesized dominant control mechanisms (loop 1: SST, xCO_2; loop 2: xCO_2, Chl-a; loop 3: SIC, SSS) within the context of the Southern Ocean's meridional overturning circulation based on current data analysis.

gas exchange through ice-mediated diffusion barriers and light limitation for photosynthesis during seasonal advance/retreat (*38*, *39*). Ice retreat releases substantial iron to surface waters (*40*), establishing shallow stratification that triggers rapid ice-edge phytoplankton blooms (*40*, *41*). This cryosphere-hydrography coupling, mediated by SSS and SIC, defines the loop's carbon dynamics.

These regional controls operate within Southern Ocean circulation, where upwelling of carbon/nutrient-rich deep waters drives CO_2 outgassing. Subsequent atmospheric modification (heating/freshening), northward Ekman transport, and subduction (e.g., Antarctic Intermediate Water formation) (*42*, *43*) facilitate the source-to-sink transition during northward transport. Our three-loop framework resolves spatial pCO_2 heterogeneity across this meridional overturning system (*44*–*46*).

The Southern Ocean's carbon cycling systems exhibit distinct responses to rising atmospheric CO_2: The Antarctic loop demonstrates sea ice–coupled regulation of air-sea CO_2 fluxes, where ice-ocean dynamics dominate long-term variations; the polar front loop shows progressive narrowing of the ocean-atmosphere pCO_2 gradient, suggesting potential conversion from a natural CO_2 source to sink under sustained CO_2 increases; whereas the subpolar system transitions from temperature-driven seasonal pCO_2 fluctuations to atmospheric CO_2-dominated control, consequently amplifying its carbon sink capacity.

The proposed three-loop pattern establishes a mechanistic framework explaining Southern Ocean pCO_2 heterogeneity, revealing distinct hierarchical controls: Cryosphere-freshwater interactions dominate the Antarctic loop, air-sea-biological coupling governs the polar front loop, whereas solubility-mesoscale processes regulate the subpolar system (Fig. 4D). This integrated perspective clarifies regional feedback to climate variability and anthropogenic forcing, critical for projecting changes in the Southern Ocean's global CO_2 sink capacity. This three-loop schematic should be regarded as a conceptual model and working hypothesis that synthesizes current observations, which future studies are encouraged to test and refine.

Implications

Enabled by the unprecedented winter coverage of satellite LIDAR, our study makes two principal contributions: We reveal that winter CO_2 outgassing south of 50°S was previously underestimated by up to 40%, and we propose a previously unknown "three-loop" framework that mechanistically explains the latitudinal controls on surface pCO_2. These findings carry profound implications for our understanding of the Southern Ocean's role in the global carbon cycle and for the future direction of climate research.

This work highlights the transformative advantage of active remote sensing, specifically spaceborne LIDAR, for observing polar carbon cycles (*47*). Unlike passive optical instruments that fail during polar night and under persistent cloud cover, LIDAR provides direct, self-illuminated measurements, overcoming a fundamental barrier that has long biased our view of high-latitude systems. This capability is not limited to the Southern Ocean; other chronically undersampled regions, such as the Arctic Ocean and cloudy equatorial zones, stand to benefit from the global deployment of LIDAR-based observing systems. Our study serves as a powerful proof-of-concept for a new era of ocean observation, paving the way for synergy with future satellite missions like the proposed Cloud-Aerosol LIDAR and Infrared Pathfinder Satellite Observations for Oceanography and Geosciences Applications (CALIGOLA) (*48*) and Guanlan (*49*).

The consequences of rectifying the winter observational gap are profound. A weaker or more variable Southern Ocean carbon sink directly affects the global carbon budget assessments maintained by bodies like the Intergovernmental Panel on Climate Change (IPCC), potentially requiring adjustments to climate projections and national emission targets. By underestimating winter outgassing, previous analyses have not only miscalculated the net annual sink but also obscured the true seasonal dynamics. This introduces systematic errors into Earth system models, which rely on observational data for calibration and validation, thereby compromising their ability to accurately project future carbon-climate feedbacks.

Despite these advances, our methodology has limitations that warrant discussion. The primary constraint is the ongoing scarcity of in situ winter pCO_2 measurements, which limits our ability to independently validate satellite-derived fluxes across all high-latitude regions. Furthermore, the current 1°-by-1° spatial resolution of our product, while sufficient for basin-scale analysis, cannot resolve the mesoscale and submesoscale features known to be hotspots of air-sea exchange. Future work must prioritize integrating LIDAR retrievals with data from winter-capable platforms like the Biogeochemical (BGC)–Argo float network (*48*, *49*) and fusing them with high-resolution datasets from ICESat-2 (Ice, Cloud, and land Elevation Satellite-2) altimetry missions to enhance flux estimates at finer scales.

Last, our findings point toward a necessary reorientation in the study and monitoring of the Southern Ocean carbon cycle. First, the demonstrated importance of wintertime processes and their control mechanisms demands that future research efforts prioritize full seasonal coverage, especially in high-latitude regions (*50*, *51*). The reliance on observations must give way to year-round, multiplatform monitoring strategies that combine active remote sensing, passive satellites, autonomous ocean platforms, and ship-based campaigns. Only through this integrated approach can we resolve the true magnitude and variability of air-sea CO_2 fluxes on relevant spatial and temporal scales. Second, the emergence of a three-loop latitudinal control framework suggests a shift from empirical flux parameterizations toward mechanism-based modeling that explicitly represents the interactions among ocean physics, biogeochemistry, and atmospheric forcing. Embedding such process-based knowledge into the next generation of ocean biogeochemistry modules within Earth System Models will enhance the realism of projections and allow for improved attribution of future carbon cycle changes. Third, our results call for closer coupling of the atmospheric and oceanic carbon communities. The cross-boundary influence of Southern Ocean outgassing on atmospheric CO_2 variability, and the feedback to climate drivers like the SAM, highlights the need for joint analysis frameworks that span the air-sea interface. Ultimately, the Southern Ocean cannot be fully understood in isolation; it must be treated as a coupled system, embedded within both the global climate system and the anthropogenic carbon budget. To that end, this effort should aim to unify LIDAR missions, BGC-Argo networks, high-resolution models, and atmospheric inversion systems under a common framework (*52*, *53*), thereby resolving the long-standing uncertainty surrounding one of Earth's most dynamic and climate-critical carbon reservoirs.

MATERIALS AND METHODS

Data acquisition and processing

Surface ocean pCO_2 data

Gridded monthly sea surface fCO_2 data were sourced from the Surface Ocean CO_2 Atlas version 2022 (SOCATv2022; www.socat.info), a comprehensive, quality-controlled database compiling global observations

from various platforms, including ships, moorings, and drifters. Our analysis focused on the period 2007–2020, which included 92.53% of the database records, ensuring robust spatiotemporal coverage. The fCO_2 values (in microatmosphere) were converted to partial pressure pCO_2 values (in microatmosphere) using the standard formulation that accounts for the nonideal behavior of CO_2 gas in seawater

$$pCO_2 = fCO_2 \cdot \exp \times \left(p\frac{(B+2\theta)}{RT} \right)^{-1} \quad (1)$$

In this equation, p represents the total atmospheric surface pressure (in pascal) obtained from the National Centers for Environmental Prediction (NCEP) reanalysis, B and θ are the virial coefficients that depend on temperature and SSS, R is the universal gas constant, and T is the absolute SST (in kelvin).

Satellite LIDAR data and preprocessing (CALIOP)

To capture year-round ocean conditions, especially during polar winter, we used observations from the CALIOP instrument onboard the CALIPSO satellite. We processed 16,236 tracks of CALIOP Level-1B V4.10 data (containing calibrated attenuated backscatter profiles at 532 nm) and Level-2 Merged Layer V4.20 products acquired between 2006 and 2023. In this study, we adopted a threshold of 120 m for surface determination, using the "Surface_Elevation" parameter from CALIOP Level 1 data, which is derived from the CloudSat science team digital elevation model and represents the surface elevation at the laser footprint above local mean sea level. CALIOP measures the intensity of backscattered light, separating it into components polarized parallel and perpendicular to the emitted laser pulse via a polarization beam splitter (PBS) and detecting these components with sensitive photomultiplier tubes.

The raw ocean backscatter signals require careful preprocessing to correct for instrument artifacts. First, the transient response of the detectors, which can cause signal overshoot after strong returns (like the ocean surface), was corrected via deconvolution via the instrument's impulse response function matrix (*27*)

$$\beta'(z) = [\mathbf{F}]^{-1}\beta(z) \quad (2)$$

where $\beta'(z)$ is the corrected backscatter signal, $\beta(z)$ denotes the measured signal, and $[\mathbf{F}]^{-1}$ represents the transient response matrix (*27*). Second, imperfections in the PBS leading to polarization cross-talk were corrected via established coefficients applied to the transient-corrected parallel and perpendicular signals to yield the final corrected signals via Eqs. 3 and 4

$$\beta_{\parallel,c} = \frac{\beta_{\parallel,m}}{1 - CT} \quad (3)$$

$$\beta_{\perp,c} = \beta_{\perp,m} - CT \times \beta_{\parallel,c} \quad (4)$$

where $\beta_{\parallel,c}$ and $\beta_{\perp,c}$ are the cross-talk–corrected parallel and vertical signals, respectively; $\beta_{\parallel,m}$ and $\beta_{\perp,m}$ are the transient-corrected signals; and CT is the cross-talk coefficient (*54*).

From these corrected signals, the total column-integrated depolarization ratio (δ_T) was calculated (*55*). The subsurface cross-polarized backscatter component, which is related to the concentration of suspended particles and thus Chl-a, was derived via δ_T and an estimate of the LIDAR surface backscatter

$$\beta_W = \delta_T \frac{\beta_S}{1 - 10\delta_T} \quad (5)$$

where β_W is the LIDAR surface backscatter estimated from the wind speed data (*22*, *24*). To exclude sea ice and ensure data quality, only measurements with $\delta_T < 0.05$ and integrated attenuated backscatter $<0.017\ sr^{-1}$ are retained, and the wind speed is constrained to 2 to 9 m/s to minimize surface foam interference (*24*, *27*).

LIDAR-derived Chl-a and supporting parameters

We used a specialized two-branch, two-step deep learning model to retrieve Chl-a, particulate backscatter (b_{bp}), and the diffuse attenuation coefficient (K_d) from the fully processed CALIOP LIDAR signals and derived parameters (*56*, *57*). In our previous publication using CALIOP data, we validated LIDAR satellite-retrieved b_{bp}, K_d, and Chl-a values using coincident Argo-based field measurements (*58*, *59*). This model architecture combines a convolutional neural network branch processing waveform data (22 variables) with a fully connected layer branch processing physical parameters (δ_T and β_W). The features from both branches are concatenated and passed through regression layers via rectified linear unit activation functions (except for the final linear output layer) (*60*). The model is trained on 10^6 monthly match points (70% training, 15% validation/evaluation) and validated against BGC-Argo data (25-km^2, 24-hour window), achieving high correlation (R = 0.85 to 0.95) and low root mean square deviation (RMSD). The model was optimized via the RMSprop algorithm (*61*) and trained/validated on a large dataset (10^6 monthly points) matched with satellite ocean color data and evaluated against independent BGC-Argo float data (within a 25-km, 24-hour window), which demonstrated high accuracy (R = 0.85 to 0.95; low RMSD). Wind speed estimates, derived from the LIDAR surface return, were also generated as part of this processing pipeline. In addition, we used integrated passive remote sensing data and reanalyzed data, including physical drivers (SST, SSS, and MLD) and atmospheric forcing (xCO_2), to modulate sea-air CO_2 exchange (*61*–*63*). Complementary datasets for sea surface pCO_2 reconstruction were obtained (see the Supplementary Materials for details). For the flux calculations, ancillary datasets, including surface barometric pressure and 10-m winds, were incorporated. All parameters were regridded to a 1°-by-1° resolution prior to analysis. The SAM index is derived as the leading principal component of monthly 700-hPa geopotential height anomalies (1958–2004) south of 20°S and is calculated from the National Centers for Environmental Prediction/National Center for Atmospheric Research (NCEP/NCAR) reanalysis dataset. The index is standardized by demeaning and normalizing to unit variance. Given the SAM's limited seasonal amplitude (*64*, *65*), we use panseasonal observations for index construction.

Neural network reconstruction of surface pCO_2

To generate comprehensive, gap-free surface ocean pCO_2 fields covering the Southern Ocean year-round, we developed and used a novel machine learning methodology based on a feed-forward neural network (FNN) (fig. S3), herein referred to as FNN-LID (*66*). An FNN was used because it is sufficient to capture the nonlinear relationships in monthly mean pCO_2 while remaining computationally efficient and robust against overfitting. This approach is designed to capture the complex, nonlinear relationships between surface pCO_2 and key environmental predictor variables derived from satellite and in situ observations (table S1). The reconstruction follows a two-step architecture:

1) Baseline climatology generation: An initial FNN was trained to estimate the monthly climatological mean field of surface pCO_2. This network uses satellite-derived monthly averages of environmental parameters, specifically, SST, SSS, Chl-a, MLD, and the atmospheric CO_2 mole fraction (xCO_2), as inputs, which are mapped against established global pCO_2 climatology data [e.g., Takahashi *et al.* (*31*)].

2) Anomaly reconstruction: A second FNN was trained to reconstruct the monthly pCO_2 anomalies (deviations from the baseline climatology). This network used contemporaneous in situ pCO_2 measurements from observational databases (primarily SOCAT) along with the same suite of monthly environmental predictor variables used in the first step. This allows the model to capture real-world interannual variability and regional features not present in the long-term mean climatology.

The final gap-filled pCO_2 estimate for any given month and location is obtained by summing the outputs from the baseline climatology network (step 1) and the anomaly reconstruction network (step 2). The key innovation enabling year-round reconstruction, particularly at high latitudes, is the integration of data derived from the CALIPSO satellite LIDAR within the FNN-LID framework. As detailed previously (see the "Data acquisition and processing" section), LIDAR provides unique day-night measurements related to Chl-a (via particulate backscatter) and SSW, which are crucially unaffected by solar illumination limitations that cause large data gaps for passive ocean color sensors during polar winter. These LIDAR-derived Chl-a and wind speed data were incorporated as vital input predictor variables into the FNNs for both reconstruction steps. Their inclusion significantly enhances data availability during winter darkness and cloudy conditions, thereby improving the robustness and reliability of the reconstructed monthly mean pCO_2 fields, especially in the challenging Southern Ocean environment.

To effectively capture the distinct seasonal cycles in pCO_2 dynamics, twelve independent FNN models were developed and trained, one for each calendar month. Each monthly model used a five-layer network architecture. The combined dataset of matched in situ pCO_2 and predictor variables was partitioned into independent subsets for training (50%), evaluation (25%), and final validation (25%). The performance and validation metrics of the resulting FNN-LID pCO_2 product are detailed in the "Validation and uncertainties" section below.

Air-sea CO_2 flux calculation

The air-sea CO_2 flux (F) is a critical component of the global carbon cycle and can be estimated via the partial pressure difference method, which relates the gradient in CO_2 partial pressures between the ocean and atmosphere to the gas transfer velocity (k_w) and the solubility of CO_2 (*sol*) (*67*). We calculated F via the standard bulk gas flux formulation

$$F = k_w \times sol \times d_p \times (1 - SIC) \tag{6}$$

$$d_p = pCO_{2\_}sea - pCO_{2\_}air \tag{7}$$

where *sol* is a function of SST and SSS, which is calculated via empirical formulations (*68*), and where k_w is influenced by the wind speed, surface turbulence, and chemical enhancement (*69*). Wind speed is typically parameterized via quadratic or cubic relationships, with recent studies favoring wind speed–dependent parameterizations that account for variability in bubble-mediated transfer (*70*).

Uncertainties in flux estimates arise from spatial and temporal variability in $pCO_{2_}$sea, measurement limitations, and the choice of gas exchange parameterization (*31*). Advances in autonomous sensors and satellite-based pCO_2 products have improved spatiotemporal coverage, yet regional biases persist, particularly in high-latitude and coastal systems. To reduce errors, integrated approaches that combine in situ measurements, remote sensing, and biogeochemical models are increasingly used (*71*). The SIC modulates the hindrance of air-sea gas exchange via ice cover. To account for gas exchange through leads and fractures in the ice, SIC values exceeding 0.99 were capped at 0.99 (*72*, *73*). This method remains a cornerstone for understanding ocean-atmosphere carbon dynamics and their climate feedbacks.

To explore the spatial variability of the relative influence between the k_w and d_p, we computed their ratio, defined as

$$t = \left| \frac{k_w}{d_p} \right| \tag{8}$$

This ratio provides a normalized indicator of the balance between wind-driven gas exchange and partial pressure gradient. When $t > 1$, gas exchange in the region is predominantly controlled by wind-driven surface turbulence. In contrast, $t < 1$ indicates that the partial pressure gradient of pCO_2 between the ocean and atmosphere exerts a stronger influence on the air-sea flux.

Validation and uncertainties of the sea-air CO_2 flux estimation

In this study, we validated the global estimates of pCO_2 derived from the FNN-LID model against observed data and widely used reconstructed datasets. The observed data used for validation were derived from the unmodeled, gridded data in the SOCATv2022 gridded dataset. The results demonstrated excellent long-term agreement, with a significant coefficient of determination (r^2) of 0.8, a low root mean square error (RMSE) of 19.56 μatm (diurnal 20.29 μatm and nocturnal 19.22 μatm), and a nearly negligible overall bias of 0.09 μatm on the basis of 206, 252 matched gridded observations (fig. S4, A and B). The mean of the day and night datasets was used to represent the monthly mean sea surface pCO_2 in the Southern Ocean. No significant differences were found between daytime (RMSE of 20.29 μatm, $N = 102{,}791$) and nighttime (RMSE of 19.22 μatm, $N = 103{,}491$) reconstructions where applicable. This strong global fit was consistently observed across both open ocean and coastal regions for each individual year, exhibiting high levels of consistency, with r^2 values ranging from 0.73 to 0.90, RMSE values between 15 and 21 μatm, and an annual bias within a narrow range of ±2 μatm, indicating temporal stability without significant interannual bias trends.

Figure S4C presents the temporal mean residuals compared with the SOCAT map for each pixel. Overall, the bias was minimal, revealing minimal bias randomly distributed across most open ocean regions. However, the bias increased in regions with sparse or limited observational data (e.g., the Southern Atlantic Ocean). Regions with high spatial variability generally exhibited weaker model fits, whereas the FNN-LID model performed notably well in capturing the dynamics of less variable open ocean regions. The residual analysis confirmed the overall robustness of the method, showing no significant degradation related to data density and no evidence of hidden systematic biases.

To further validate surface ocean pCO_2 across different years, we calculate the annual mean bias (fig. S4D). Our reconstructed dataset shows no significant interannual bias trend, with the annual mean error consistently within ±0.2 μatm.

In polar regions, FNN-LID pCO_2 estimates exhibited high quality in the Antarctic (RMSE of 22.3 μatm) compared with recent SOCAT-based global pCO_2 fields (RMSEs of 26.7 μatm) and provided more accurate estimates for the polar continental shelf during winter (*74*). This advantage arises from the use of CALIPSO, which offers superior capabilities over traditional passive remote sensing systems [e.g., Sea-viewing Wide Field-of-view Sensor (SeaWiFS) or MODIS] in distinguishing between clouds and sea ice (*75*). Consequently, the active satellite LIDAR input allows for continuous observations during the winter polar night, enabling high-coverage polar data (*76*). This LIDAR-enabled, year-round data stream provides unprecedented coverage, significantly boosting the reliability of our pCO_2 fields in the Southern Ocean, especially during the critical winter months when passive sensors fail. It should be noted that the validation is primarily constrained to regions and seasons with relatively dense SOCAT observations. In particular, winter and high-latitude estimates remain less well constrained, and future validation efforts will benefit greatly from additional in situ measurements, such as those provided by BGC-Argo floats.

In conclusion, the residual analysis confirms that the global FNN-LID method meets most criteria for a robust fit, with no significant evidence of hidden biases. Notably, the estimates do not exhibit any substantial degradation with respect to data density, either temporally or spatially. Regions with pronounced spatial or temporal variability show relatively weak fits, while the method excels in accurately estimating pCO_2 for most open ocean regions characterized by lower variability. Globally, the FNN-LID model demonstrated an excellent fit with the gridded pCO_2 data from SOCATv2022, with an accuracy comparable to that of other recent models in terms of the mean monthly results. These findings further support the reliability and effectiveness of the FNN-LID approach for global pCO_2 estimation. While uncertainties in gas transfer velocity parameterizations and other factors contribute to the overall flux uncertainty, the demonstrated accuracy and enhanced spatiotemporal coverage of our reconstructed pCO_2 fields significantly reduce a major source of uncertainty, thereby increasing confidence in the resulting air-sea CO_2 flux estimates presented in this study.

Driving factor analysis

Sea surface pCO_2 is influenced by both air-sea interactions and basin-scale properties. Using a nonlinear RF approach, we quantified the relative contributions of eight factors to the spatiotemporal variability in pCO_2 in the Southern Ocean. These factors include ocean dynamic variables (SSH, SSS, SIC, and SSW), biogeochemical drivers (Chl-a, MLD, and SST), and anthropogenic influences (xCO_2). To interpret the spatial and temporal patterns of the air-sea CO_2 flux, we normalized the relative contributions of these factors and calculated them to the basis of annual mean values. The dominant driver at each grid cell was identified as the factor with the highest contribution. The feature importance in the RF model was evaluated via the Gini importance index, which is selected over the permutation and Boruta indices because of its computational efficiency, suitability for large-scale analyses, and ease of interpretation (*31*). The Gini importance reflects the mean decrease in Gini impurity, computed as the normalized sum of impurity reductions across all nodes. For each factor, its contribution ranges from 0 to 100%, with the total contributions of all eight factors summing to 100%.

Supplementary Materials

This PDF file includes:

Supplementary Text
Figs. S1 to S4
Table S1

REFERENCES AND NOTES

1. S. Khatiwala, F. Primeau, T. Hall, Reconstruction of the history of anthropogenic CO_2 concentrations in the ocean. *Nature* **462**, 346–349 (2009).
2. N. Gruber, P. Landschützer, N. S. Lovenduski, The variable Southern Ocean carbon sink. *Ann. Rev. Mar. Sci.* **11**, 159–186 (2019).
3. K. Caldeira, P. B. Duffy, The role of the Southern Ocean in uptake and storage of anthropogenic carbon dioxide. *Science* **287**, 620–622 (2000).
4. A. R. Gray, The four-dimensional carbon cycle of the Southern Ocean. *Ann. Rev. Mar. Sci.* **16**, 163–190 (2024).
5. M. B. McElroy, Marine biological controls on atmospheric CO_2 and climate. *Nature* **302**, 328–329 (1983).
6. J. Hauck, L. Gregor, C. Nissen, L. Patara, M. Hague, P. Mongwe, S. Bushinsky, S. C. Doney, N. Gruber, C. L. Quéré, M. Manizza, M. Mazloff, P. M. S. Monteiro, J. Terhaar, The Southern Ocean carbon cycle 1985–2018: Mean, seasonal cycle, trends, and storage. *Global Biogeochem. Cycles* **37**, e2023GB007848 (2023).
7. T. De Vries, C. L. Quéré, O. Andrews, S. Berthet, J. Hauck, T. Ilyina, P. Landschützer, A. Lenton, I. D. Lima, M. Nowicki, J. Schwinger, R. Séférian, Decadal trends in the ocean carbon sink. *Proc. Natl. Acad. Sci. U.S.A.* **116**, 11646–11651 (2019).
8. P. Rustogi, P. Landschützer, S. Brune, J. Baehr, The impact of seasonality on the annual air-sea carbon flux and its interannual variability. *npj Clim. Atmos. Sci.* **6**, 66 (2023).
9. D. C. E. Bakker, B. Pfeil, C. S. Landa, N. Metzl, K. M. O'Brien, A. Olsen, K. Smith, C. Cosca, S. Harasawa, S. D. Jones, S.-i. Nakaoka, Y. Nojiri, U. Schuster, T. Steinhoff, C. Sweeney, T. Takahashi, B. Tilbrook, C. Wada, R. Wanninkhof, S. R. Alin, C. F. Balestrini, L. Barbero, N. R. Bates, A. A. Bianchi, F. Bonou, J. Boutin, Y. Bozec, E. F. Burger, W.-J. Cai, R. D. Castle, L. Chen, M. Chierici, K. Currie, W. Evans, C. Featherstone, R. A. Feely, A. Fransson, C. Goyet, N. Greenwood, L. Gregor, S. Hankin, N. J. Hardman-Mountford, J. Harlay, J. Hauck, M. Hoppema, M. P. Humphreys, C. W. Hunt, B. Huss, J. S. P. Ibánhez, T. Johannessen, R. Keeling, V. Kitidis, A. Körtzinger, A. Kozyr, E. Krasakopoulou, A. Kuwata, P. Landschützer, S. K. Lauvset, N. Lefèvre, C. L. Monaco, A. Manke, J. T. Mathis, L. Merlivat, F. J. Millero, P. M. S. Monteiro, D. R. Munro, A. Murata, T. Newberger, A. M. Omar, T. Ono, K. Paterson, D. Pearce, D. Pierrot, L. L. Robbins, S. Saito, J. Salisbury, R. Schlitzer, B. Schneider, R. Schweitzer, R. Sieger, I. Skjelvan, K. F. Sullivan, S. C. Sutherland, A. J. Sutton, K. Tadokoro, M. Telszewski, M. Tuma, S. M. A. C. van Heuven, D. Vandemark, B. Ward, A. J. Watson, S. Xu, A multi-decade record of high-quality fCO_2 data in version 3 of the Surface Ocean CO_2 Atlas (SOCAT). *Earth Syst. Sci. Data* **8**, 383–413 (2016).
10. L. Gloege, G. A. Mc Kinley, P. Landschützer, A. R. Fay, T. L. Frölicher, J. C. Fyfe, T. Ilyina, S. Jones, N. S. Lovenduski, K. B. Rodgers, S. Schlunegger, Y. Takano, Quantifying errors in observationally based estimates of ocean carbon sink variability. *Global Biogeochem. Cycles* **35**, e2020GB006788 (2021).
11. J. Hauck, C. Nissen, P. Landschützer, C. Rödenbeck, S. Bushinsky, A. Olsen, Sparse observations induce large biases in estimates of the global ocean CO_2 sink: An ocean model subsampling experiment. *Philos. Trans. A Math. Phys. Eng. Sci.* **381**, 20220063 (2023).
12. A. Anav, P. Friedlingstein, M. Kidston, L. Bopp, P. Ciais, P. Cox, C. Jones, M. Jung, R. Myneni, Z. Zhu, Evaluating the land and ocean components of the global carbon cycle in the CMIP5 earth system models. *J. Climate* **26**, 6801–6843 (2013).
13. A. Lenton, B. Tilbrook, R. M. Law, D. Bakker, S. C. Doney, N. Gruber, M. Ishii, M. Hoppema, N. S. Lovenduski, R. J. Matear, B. I. McNeil, N. Metzl, S. E. Mikaloff Fletcher, P. M. S. Monteiro, C. Rödenbeck, C. Sweeney, T. Takahashi, Sea–air CO_2 fluxes in the Southern Ocean for the period 1990–2009. *Biogeosciences* **10**, 4037–4054 (2013).
14. A. Kessler, J. Tjiputra, The Southern Ocean as a constraint to reduce uncertainty in future ocean carbon sinks. *Earth Syst. Dynam.* **7**, 295–312 (2016).
15. N. P. Mongwe, M. Vichi, P. M. Monteiro, The seasonal cycle of pCO_2 and CO_2 fluxes in the Southern Ocean: Diagnosing anomalies in CMIP5 Earth system models. *Biogeosciences* **15**, 2851–2872 (2018).
16. M. Gloor, N. Gruber, J. Sarmiento, C. L. Sabine, R. A. Feely, C. Rödenbeck, A first estimate of present and preindustrial air-sea CO_2 flux patterns based on ocean interior carbon measurements and models. *Geophys. Res. Lett.* **30**, 10-1–10-4 (2003).
17. K. R. Arrigo, G. L. van Dijken, S. Bushinsky, Primary production in the Southern Ocean, 1997–2006. *J. Geophys. Res. Oceans* **113**, 1–27 (2008).

18. C. L. Quéré, C. Rödenbeck, E. T. Buitenhuis, T. J. Conway, R. Langenfelds, A. Gomez, C. Labuschagne, M. Ramonet, T. Nakazawa, N. Metzl, N. Gillett, M. Heimann, Saturation of the Southern Ocean CO_2 sink due to recent climate change. *Science* **316**, 1735–1738 (2007).
19. N. S. Lovenduski, N. Gruber, S. C. Doney, Toward a mechanistic understanding of the decadal trends in the Southern Ocean carbon sink. *Global Biogeochem. Cycles* **22**, GB3016 (2008).
20. P. Landschützer, N. Gruber, F. A. Haumann, C. Rödenbeck, D. C. E. Bakker, S. van Heuven, M. Hoppema, N. Metzl, C. Sweeney, T. Takahashi, B. Tilbrook, R. Wanninkhof, The reinvigoration of the Southern Ocean carbon sink. *Science* **349**, 1221–1224 (2015).
21. L. Gregor, S. Kok, P. Monteiro, Interannual drivers of the seasonal cycle of CO_2 in the Southern Ocean. *Biogeosciences* **15**, 2361–2378 (2018).
22. Y. Hu, K. Stamnes, M. Vaughan, J. Pelon, C. Weimer, D. Wu, M. Cisewski, W. Sun, P. Yang, B. Lin, A. Omar, D. Flittner, C. Hostetler, C. Trepte, D. Winker, G. Gibson, M. Santa-Maria, Sea surface wind speed estimation from space-based lidar measurements. *Atmos. Chem. Phys.* **8**, 3593–3601 (2008).
23. Y. Hu, D. Winker, M. Vaughan, B. Lin, A. Omar, C. Trepte, D. Flittner, P. Yang, S. L. Nasiri, B. Baum, R. Holz, W. Sun, Z. Liu, Z. Wang, S. Young, K. Stamnes, J. Huang, R. Kuehn, CALIPSO/CALIOP cloud phase discrimination algorithm. *J. Atmos. Oceanic Tech.* **26**, 2293–2309 (2009).
24. M. J. Behrenfeld, Y. Hu, C. A. Hostetler, G. Dall'Olmo, S. D. Rodier, J. W. Hair, C. R. Trepte, Space-based lidar measurements of global ocean carbon stocks. *Geophys. Res. Lett.* **40**, 4355–4360 (2013).
25. M. J. Behrenfeld, P. Gaube, A. Della Penna, R. T. O'Malley, W. J. Burt, Y. Hu, P. S. Bontempi, D. K. Steinberg, E. S. Boss, D. A. Siegel, C. A. Hostetler, P. D. Tortell, S. C. Doney, Global satellite-observed daily vertical migrations of ocean animals. *Nature* **576**, 257–261 (2019).
26. D. Winker, J. Pelon, J. Coakley Jr., S. Ackerman, R. Charlson, P. Colarco, P. Flamant, Q. Fu, R. Hoff, C. Kittaka, T. L. Kubar, H. le Treut, M. P. Mccormick, G. Mégie, L. Poole, K. Powell, C. Trepte, M. A. Vaughan, B. A. Wielicki, The CALIPSO mission: A global 3D view of aerosols and clouds. *Bull. Am. Meteorol. Soc.* **91**, 1211–1230 (2010).
27. X. Lu, Y. Hu, C. Trepte, S. Zeng, J. H. Churnside, Ocean subsurface studies with the CALIPSO spaceborne lidar. *J. Geophys. Res. Oceans* **119**, 4305–4317 (2014).
28. J. H. Churnside, B. J. McCarty, X. Lu, Subsurface ocean signals from an orbiting polarization lidar. *Remote Sens* **5**, 3457–3475 (2013).
29. M. J. Behrenfeld, Y. Hu, R. T. O'Malley, E. S. Boss, C. A. Hostetler, D. A. Siegel, J. L. Sarmiento, J. Schulien, J. W. Hair, X. Lu, S. Rodier, A. J. Scarino, Annual boom–bust cycles of polar phytoplankton biomass revealed by space-based lidar. *Nat. Geosci.* **10**, 118–122 (2017).
30. K. Bisson, E. Boss, P. Werdell, A. Ibrahim, M. Behrenfeld, Particulate backscattering in the global ocean: A comparison of independent assessments. *Geophys. Res. Lett.* **48**, e2020GL090909 (2021).
31. T. Takahashi, S. C. Sutherland, R. Wanninkhof, C. Sweeney, R. A. Feely, D. W. Chipman, B. Hales, G. Friederich, F. Chavez, C. Sabine, A. Watson, D. C. E. Bakker, U. Schuster, N. Metzl, H. Yoshikawa-Inoue, M. Ishii, T. Midorikawa, Y. Nojiri, A. Körtzinger, T. Steinhoff, M. Hoppema, J. Olafsson, T. S. Arnarson, B. Tilbrook, T. Johannessen, A. Olsen, R. Bellerby, C. S. Wong, B. Delille, N. R. Bates, H. J. W. de Baar, Climatological mean and decadal change in surface ocean pCO_2, and net sea–air CO_2 flux over the global oceans. *Deep-Sea Res. II Top. Stud. Oceanogr.* **56**, 554–577 (2009).
32. P. Landschützer, N. Gruber, D. C. Bakker, Decadal variations and trends of the global ocean carbon sink. *Global Biogeochem. Cycles* **30**, 1396–1417 (2016).
33. N. Gruber, D. C. E. Bakker, T. DeVries, L. Gregor, J. Hauck, P. Landschützer, G. A. McKinley, J. D. Müller, Trends and variability in the ocean carbon sink. *Nat. Rev. Earth Environ.* **4**, 119–134 (2023).
34. N. S. Lovenduski, N. Gruber, S. C. Doney, I. D. Lima, Enhanced CO_2 outgassing in the Southern Ocean from a positive phase of the Southern Annular Mode. *Global Biogeochem. Cycles* **21**, (2007).
35. J. Hauck, C. Völker, D. A. Wolf-Gladrow, C. Laufkötter, M. Vogt, O. Aumont, L. Bopp, E. T. Buitenhuis, S. C. Doney, J. Dunne, N. Gruber, T. Hashioka, J. John, C. L. Quéré, I. D. Lima, H. Nakano, R. Séférian, I. Totterdell, On the Southern Ocean CO_2 uptake and the role of the biological carbon pump in the 21st century. *Global Biogeochem. Cycles* **29**, 1451–1470 (2015).
36. J. K. Moore, W. Fu, F. Primeau, G. L. Britten, K. Lindsay, M. Long, S. C. Doney, N. Mahowald, F. Hoffman, J. T. Randerson, Sustained climate warming drives declining marine biological productivity. *Science* **359**, 1139–1143 (2018).
37. C. Laufkötter, N. Gruber, Will marine productivity wane? *Science* **359**, 1103–1104 (2018).
38. M. Hoppema, W. Roether, R. G. Bellerby, H. J. de Baar, Direct measurements reveal insignificant storage of anthropogenic CO_2 in the abyssal Weddell Sea. *Geophys. Res. Lett.* **28**, 1747–1750 (2001).
39. B. J. Butterworth, S. D. Miller, Air-sea exchange of carbon dioxide in the Southern Ocean and Antarctic marginal ice zone. *Geophys. Res. Lett.* **43**, 7223–7230 (2016).
40. D. Lannuzel, M. Vancoppenolle, P. van der Merwe, J. de Jong, K. M. Meiners, M. Grotti, J. Nishioka, V. Schoemann, Iron in sea ice: Review and new insights. *Elementa* **4**, 000130 (2016).
41. W. O. Smith Jr., J. C. Comiso, Influence of sea ice on primary production in the Southern Ocean: A satellite perspective. *J. Geophys. Res. Oceans* **113**, 1–19 (2008).
42. S. Mikaloff Fletcher, N. Gruber, A. R. Jacobson, M. Gloor, S. Doney, S. Dutkiewicz, M. Gerber, M. Follows, F. Joos, K. Lindsay, D. Menemenlis, A. Mouchet, S. A. Müller, J. L. Sarmiento, Inverse estimates of the oceanic sources and sinks of natural CO_2 and the implied oceanic carbon transport. *Global Biogeochem. Cycles* **21**, (2007).
43. P. W. Boyd, A. J. Watson, C. S. Law, E. R. Abraham, T. Trull, R. Murdoch, D. C. Bakker, A. R. Bowie, K. Buesseler, H. Chang, M. Charette, P. Croot, K. Downing, R. Frew, M. Gall, M. Hadfield, J. Hall, M. Harvey, G. Jameson, J. LaRoche, M. Liddicoat, R. Ling, M. T. Maldonado, R. M. McKay, S. Nodder, S. Pickmere, R. Pridmore, S. Rintoul, K. Safi, P. Sutton, R. Strzepek, K. Tanneberger, S. Turner, A. Waite, J. Zeldis, A mesoscale phytoplankton bloom in the polar Southern Ocean stimulated by iron fertilization. *Nature* **407**, 695–702 (2000).
44. L. Bopp, M. Lévy, L. Resplandy, J.-B. Sallée, Pathways of anthropogenic carbon subduction in the global ocean. *Geophys. Res. Lett.* **42**, 6416–6423 (2015).
45. N. Gruber, J. L. Sarmiento, "Large-scale biogeochemical-physical interactions in elemental cycles" in *The Sea*, vol. 12 (John Wiley & Sons, Inc., 2002); pp. 337–399.
46. J.-B. Sallée, R. J. Matear, S. R. Rintoul, A. Lenton, Localized subduction of anthropogenic carbon dioxide in the Southern Hemisphere oceans. *Nat. Geosci.* **5**, 579–584 (2012).
47. T. Markus, T. Neumann, A. Martino, W. Abdalati, K. Brunt, B. Csatho, S. Farrell, H. Fricker, A. Gardner, D. Harding, M. Jasinski, R. Kwok, L. Magruder, D. Lubin, S. Luthcke, J. Morison, R. Nelson, A. Neuenschwander, S. Palm, S. Popescu, C. K. Shum, B. E. Schutz, B. Smith, Y. Yang, J. Zwally, The Ice, Cloud, and land Elevation Satellite-2 (ICESat-2): Science requirements, concept, and implementation. *Remote Sens. Environ.* **190**, 260–273 (2017).
48. M. J. Behrenfeld, L. Lorenzoni, Y. Hu, K. M. Bisson, C. A. Hostetler, P. Di Girolamo, D. Dionisi, F. Longo, S. Zoffoli, Satellite lidar measurements as a critical new global ocean climate record. *Remote Sens* **15**, 5567 (2023).
49. G. Chen, J. Tang, C. Zhao, S. Wu, L. Wu, Concept design of the "Guanlan" science mission: China's novel contribution to space oceanography. *Front. Mar. Sci.* **6**, 194 (2019).
50. G. Griffiths, R. Davis, C. Eriksen, D. Frye, P. Marchand, T. Dickey, R. Weller, "Towards new platform technology for sustained observations" in *Observing the Oceans in the 21st Century* (Australian Bureau of Meteorology; 2001); pp. 324–338.
51. L. M. Djeutchouang, N. Chang, L. Gregor, M. Vichi, P. M. Monteiro, The sensitivity of pCO_2 reconstructions to sampling scales across a Southern Ocean sub-domain: A semi-idealized ocean sampling simulation approach. *Biogeosciences* **19**, 4171–4195 (2022).
52. C. Jamet, B. Mj, D. Ab, K. Ov, A. Ibrahim, Z. Ahmad, F. Angelini, M. Babin, M. J. Behrenfeld, E. Boss, B. Cairns, J. Churnside, J. Chowdhary, A. Davis, D. Dionisi, L. Duforêt-Gaurier, B. Franz, R. Frouin, M. Gao, A. Gilerson, Going beyond standard ocean color observations: Lidar and polarimetry. *Front. Mar. Sci.* **6**, 10.3389/fmars.2019.00251 (2019).
53. C. A. Hostetler, M. J. Behrenfeld, Y. Hu, J. W. Hair, J. A. Schulien, Spaceborne lidar in the study of marine systems. *Ann. Rev. Mar. Sci.* **10**, 121–147 (2018).
54. X. Lu, Y. Hu, Y. Yang, T. Neumann, A. Omar, R. Baize, M. Vaughan, S. Rodier, B. Getzewich, P. Lucker, C. Trepte, C. Hostetler, D. Winker, New ocean subsurface optical properties from space lidars: CALIOP/CALIPSO and ATLAS/ICESat-2. *Earth Space Sci.* **8**, e2021EA001839 (2021).
55. D. Dionisi, V. E. Brando, G. Volpe, S. Colella, R. Santoleri, Seasonal distributions of ocean particulate optical properties from spaceborne lidar measurements in Mediterranean and Black sea. *Remote Sens. Environ.* **247**, 111889 (2020).
56. Q. Kong, R. Wang, W. R. Walter, M. Pyle, K. Koper, B. Schmandt, Combining deep learning with physics based features in explosion-earthquake discrimination. *Geophys. Res. Lett.* **49**, e2022GL098645 (2022).
57. Z. Zhang, S. Zhang, M. J. Behrenfeld, P. Chen, C. Jamet, P. Di Girolamo, D. Dionisi, Y. Hu, X. Lu, Y. Pan, Combining deep learning with physical parameters in POC and PIC inversion from spaceborne lidar CALIOP. *ISPRS J. Photogramm. Remote Sens.* **212**, 193–211 (2024).
58. Z. Zhang, S. Zhang, M. J. Behrenfeld, C. Jamet, P. Di Girolamo, D. Dionisi, Y. Hu, X. Lu, Y. Pan, M. Luo, H. Huang, D. Pan, P. Chen, Consistency analysis of water diffuse attenuation between ICESat-2 and MODIS in marginal sea: A case study in China Sea. *Remote Sens. Environ.* **318**, 114602 (2025).
59. Z. Zhang, P. Chen, C. Jamet, D. Dionisi, Y. Hu, X. Lu, D. Pan, Retrieving bbp and POC from CALIOP: A deep neural network approach. *Remote Sens. Environ.* **287**, 113482 (2023).
60. Y. LeCun, Y. Bengio, G. Hinton, Deep learning. *Nature* **521**, 436–444 (2015).
61. A. Denvil-Sommer, M. Gehlen, M. Vrac, C. Mejia, LSCE-FFNN-v1: A two-step neural network model for the reconstruction of surface ocean pCO_2 over the global ocean. *Geosci. Model Dev.* **12**, 2091–2105 (2019).
62. P. Landschützer, N. Gruber, D. C. Bakker, U. Schuster, S. Nakaoka, M. R. Payne, T. P. Sasse, J. Zeng, A neural network-based estimate of the seasonal to inter-annual variability of the Atlantic Ocean carbon sink. *Biogeosciences* **10**, 7793–7815 (2013).
63. L. Gregor, A. D. Lebehot, S. Kok, P. M. Scheel Monteiro, A comparative assessment of the uncertainties of global surface ocean CO_2 estimates using a machine-learning ensemble (CSIR-ML6 version 2019a)–Have we hit the wall? *Geosci. Model Dev.* **12**, 5113–5136 (2019).
64. D. L. Hartmann, F. Lo, Wave-driven zonal flow vacillation in the Southern Hemisphere. *J. Atmos. Sci.* **55**, 1303–1315 (1998).
65. A. Hall, M. Visbeck, Synchronous variability in the Southern Hemisphere atmosphere, sea ice, and ocean resulting from the annular mode. *J. Climate* **15**, 3043–3057 (2002).

66. S. Zhang, P. Chen, Y. Hu, Z. Zhang, C. Jamet, X. Lu, D. Dionisi, D. Pan, Diurnal global ocean surface pCO_2 and air–sea CO_2 flux reconstructed from spaceborne LiDAR data. *PNAS Nexus* **3**, pgad432 (2024).
67. R. Wanninkhof, G.-H. Park, T. Takahashi, C. Sweeney, R. Feely, Y. Nojiri, N. Gruber, S. C. Doney, G. A. McKinley, A. Lenton, Global ocean carbon uptake: Magnitude, variability and trends. *Biogeosciences* **10**, 1983–2000 (2013).
68. R. F. Weiss, Carbon dioxide in water and seawater: The solubility of a non-ideal gas. *Mar. Chem.* **2**, 203–215 (1974).
69. P. D. Nightingale, G. Malin, C. S. Law, A. J. Watson, P. S. Liss, M. I. Liddicoat, J. Boutin, R. C. Upstill-Goddard, In situ evaluation of air-sea gas exchange parameterizations using novel conservative and volatile tracers. *Global Biogeochem. Cycles* **14**, 373–387 (2000).
70. D. T. Ho, C. S. Law, M. J. Smith, P. Schlosser, M. Harvey, P. Hill, Measurements of air-sea gas exchange at high wind speeds in the Southern Ocean: Implications for global parameterizations. *Geophys. Res. Lett.* **33**, e2006GL026817 (2006).
71. C. Rödenbeck, R. F. Keeling, D. C. Bakker, N. Metzl, A. Olsen, C. Sabine, M. Heimann, Global surface-ocean p^{CO_2} and sea–air CO_2 flux variability from an observation-driven ocean mixed-layer scheme. *Ocean Sci.* **9**, 193–216 (2013).
72. J. Prytherch, I. M. Brooks, P. M. Crill, B. F. Thornton, D. J. Salisbury, M. Tjernström, L. G. Anderson, M. C. Geibel, C. Humborg, Direct determination of the air-sea CO_2 gas transfer velocity in Arctic sea ice regions. *Geophys. Res. Lett.* **44**, 3770–3778 (2017).
73. I. Semiletov, A. Makshtas, S. I. Akasofu, E. L. Andreas, Atmospheric CO_2 balance: The role of Arctic sea ice. *Geophys. Res. Lett.* **31**, L05121 (2004).
74. S. Zhang, P. Chen, Z. Zhang, D. Pan, Carbon air–sea flux in the Arctic Ocean from CALIPSO from 2007 to 2020. *Remote Sens* **14**, 6196 (2022).
75. M. Babin, K. Arrigo, S. Bélanger, M.-H. Forget, *Ocean Colour Remote Sensing in Polar Seas* (IOCCG, 2015).
76. Y. Liu, S. A. Ackerman, B. C. Maddux, J. R. Key, R. A. Frey, Errors in cloud detection over the Arctic using a satellite imager and implications for observing feedback mechanisms. *J. Climate* **23**, 1894–1907 (2010).

Acknowledgments: We acknowledge NASA, SOCAT, European Centre for Medium Range Weather Forecasts, NCEP, and Copernicus Marine Environment Monitoring Service for providing in situ pCO_2 data and satellite and reanalysis data. **Funding:** This study was supported by the National Natural Science Foundation of China (grant no. 42425102 to K.S.; grant no. 42322606; grant no. 42276180; grant no. W2521002 to P.C.; and grant no. 4240060663 to S.Z.), Zhejiang Provincial Natural Science Foundation (grant no. LZ25D060001 to P.C.), and National Key Research and Development Program of China (grant no. 2022YFB3901703; and grant no. 2022YFB3902603 to P.C.). **Author contributions:** S.Z., P.C., and K.S. conceived the study and prepared the original manuscript. Z.Z., S.Z., and D.P. provided parts of data. K.B., C.J., P.D.G., D.D., and Y.H. prepared and/or revised the manuscript. **Competing interests:** The authors declare that they have no competing interests. **Data and materials availability:** All data needed to evaluate the conclusions in the paper are present in the paper and/or the Supplementary Materials as well as from Zenodo at https://zenodo.org/records/16959375.

Submitted 23 June 2025
Accepted 6 October 2025
Published 5 November 2025
10.1126/sciadv.aea0024

ScienceAdvances

Substantially underestimated winter CO_2 sources of the Southern Ocean

Siqi Zhang, Peng Chen, Kelsey Bisson, Cédric Jamet, Paolo Di Girolamo, Davide Dionisi, Yongxiang Hu, Zhenhua Zhang, Kun Shi, and Delu Pan

Sci. Adv. **11** (45), eaea0024. DOI: 10.1126/sciadv.aea0024